
Efficient remedies for outlier detection with variational autoencoders

Kushal Chauhan¹, Pradeep Shenoy¹, Manish Gupta¹, and Devarajan Sridharan²

¹Google Research

{kushalchauhan, shenoypradeep, manishgupt}@google.com

²Center for Neuroscience, Indian Institute of Science

sridhar@iisc.ac.in

Abstract

Deep networks often make confident, yet incorrect, predictions when tested with outlier data that is far removed from their training distributions. Likelihoods computed by deep generative models are a candidate metric for outlier detection with unlabeled data. Yet, previous studies have shown that such likelihoods are unreliable and can be easily biased by simple transformations to input data. Here, we examine outlier detection with variational autoencoders (VAEs), among the simplest class of deep generative models. First, we show that a theoretically-grounded correction readily ameliorates a key bias with VAE likelihood estimates. The bias correction is model-free, sample-specific, and accurately computed with the Bernoulli and continuous Bernoulli visible distributions. Second, we show that a well-known preprocessing technique, contrast normalization, extends the effectiveness of bias correction to natural image datasets. Third, we show that the variance of the likelihoods computed over an ensemble of VAEs also enables robust outlier detection. We perform a comprehensive evaluation of our remedies with nine (grayscale and natural) image datasets, and demonstrate significant advantages, in terms of both speed and accuracy, over four other state-of-the-art methods. Our lightweight remedies are biologically inspired and may serve to achieve efficient outlier detection with many types of deep generative models.

1 Introduction

Deep neural networks are increasingly deployed in real-world computer vision applications. A key issue with such deployments is over-confident predictions: the tendency of these networks to make confident, yet incorrect, predictions when tested with images whose statistics are far removed from the training data distribution [26]. Developing robust methods for outlier detection is, therefore, an important challenge with critical real-world implications.

A popular class of approaches for outlier detection, especially with label-free data, involves computing sample likelihoods with deep generative models like variational autoencoders (VAEs [9]) or flow-based models (e.g. Glow [8]). Here, we explore outlier detection with VAEs, arguably among the simplest of deep generative models. In VAEs, both the generative model $p_{\theta}(\mathbf{x}|\mathbf{z})$ and the inference model $q_{\phi}(\mathbf{z}|\mathbf{x})$ are parameterized by deep neural networks with parameters θ (decoder) and ϕ (encoder) respectively; the stochastic latent representation \mathbf{z} is typically of considerably lower dimensionality than the input data \mathbf{x} . VAEs differ from other kinds of deep generative models, like flow models, in that rather than directly optimizing the marginal likelihood $p(\mathbf{x})$, they seek to optimize the evidence lower bound (ELBO) as a proxy for maximizing $p(\mathbf{x})$.

Several previous studies have shown that likelihoods computed by deep generative models, including VAEs, are unreliable for outlier detection [23, 18, 3, 30]. For example, these likelihoods are readily

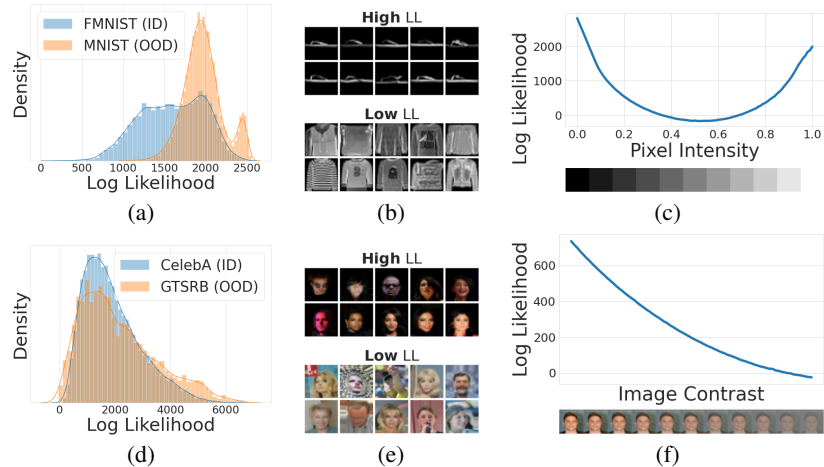


Figure 1: **VAE likelihoods are unreliable for outlier detection.** (a) Fashion-MNIST VAE assigns higher log-likelihoods to out-of-distribution (OOD) MNIST samples, as compared to in-distribution (ID) Fashion-MNIST samples. (b) Top and bottom rows: Fashion-MNIST images assigned highest and lowest log-likelihoods, respectively, by the Fashion-MNIST VAE. (c) Fashion-MNIST VAE log-likelihoods, based on the continuous Bernoulli visible distribution, for simulated images with uniform pixel intensities ranging from full-black to full-white. (d) Same as in panel (a), but for CelebA VAE, which assigns comparable likelihoods to both out-of-distribution GTSRB samples and in-distribution CelebA samples. (e) Same as in panel (b) but samples assigned highest (top row) and lowest (bottom row) likelihoods by the CelebA VAE. (f) CelebA VAE log-likelihoods, based on the continuous Bernoulli visible distribution, for simulated images with varying contrasts (high to low).

biased by differences in low-level image statistics, like the number of zeros in a sample [23] or the variance in the distribution of pixel intensities [18]. A few solutions have been proposed to overcome these challenges. However, these suffer from computational bottlenecks [23, 30] or theoretical limitations [3], or do not work well in low-sample regimes [17] (see Section 5, Related Work).

In this context, we propose and test three efficient, biologically-inspired remedies that achieve or approach state-of-the-art for outlier detection, both with grayscale and natural image datasets. Our key contributions are as follows:

- We present a theoretically-grounded and easy-to-compute bias correction for VAE likelihoods. This bias correction achieves state-of-the-art outlier detection with multiple grayscale datasets.
- We show that a standard preprocessing step – contrast normalization – enables bias correction to achieve state-of-the-art accuracies also with multiple natural image datasets.
- We develop an ensemble score – the variance of the log-likelihoods across an ensemble of VAEs – that is effective for outlier detection with both types of data.
- We present, to the best of our knowledge, the most comprehensive evaluation of outlier detection with VAEs to date, with nine datasets in all, demonstrating key advantages in terms of both speed and accuracy over four other competing, state-of-the-art approaches [25, 23, 30, 3].

In summary, we propose lightweight and computationally efficient remedies that achieve robust outlier detection with VAEs. These remedies may also be relevant for outlier detection with other classes of deep generative models [24].

2 The challenge with outlier detection using VAE likelihoods

We illustrate the challenge of outlier detection with VAE likelihoods, by taking a fresh look at two previously reported sources of bias [23, 18].

Bias arising from pixel intensity. As a first example, we train a VAE with grayscale Fashion-MNIST images (fashion product thumbnails [29]) and compute the likelihood for both in-distribution and out-of-distribution (MNIST, handwritten digits [13]), test samples. The VAE architecture and training details are described in Appendix A. Unless otherwise stated, we use the recently published

continuous Bernoulli distribution [16] as the visible distribution. We replicate the well-known issue with VAE likelihoods: the VAE trained with Fashion-MNIST samples assigns higher likelihoods, overall, to out-of-distribution (MNIST) samples as compared to in-distribution (Fashion-MNIST) samples (Fig. 1a).

We explore a previously reported claim that the number of zero-valued pixels biases VAE likelihoods toward higher values [23]. We plot samples from Fashion-MNIST dataset that are assigned the highest and lowest likelihoods by the VAE. Indeed, the highest VAE likelihoods are typically assigned to samples with a large number of black pixels (Fig. 1b, top row), whereas the lowest likelihoods are assigned to samples with many intermediate (gray) pixel values (Fig. 1b, bottom row). To study this bias further, we create simulated images with uniform pixel intensities varying monotonically over a wide range. We observe a systematic, U-shaped, variation in VAE likelihoods with pixel intensities: the highest likelihoods occur for the darkest and brightest images, with lower likelihood values for images of intermediate gray intensities (Fig. 1c). In other words, pixel intensities bias VAE likelihoods systematically.

Bias arising from channel variance or image contrast. As a second example, we train a VAE with natural images from the CelebA dataset (celebrity faces, cropped [15]) as in-distribution data and compute the likelihood for samples from the GTSRB dataset (traffic signs, [27]) as out-of-distribution data. Again, we replicate the well-known issue with VAE likelihoods: CelebA VAE likelihoods are comparable, and sometimes higher, for out-of-distribution GTSRB samples, as compared to in-distribution CelebA samples (Fig. 1d).

We explore a previously reported claim that differences in the per-channel variance between datasets lead to biases in VAE likelihoods [18]. As before, we plot samples from CelebA dataset that are assigned the highest and lowest likelihoods by the CelebA VAE. Faces with dark backgrounds (including dark hair shades) and high contrast between the face and background are assigned the highest likelihoods (Fig. 1e, top row). On the other hand, faces with light backgrounds (including light hair shades) and comparatively lower contrast between the face and background are assigned the lowest likelihoods (Fig. 1e, bottom row). Again, we create simulated images by systematically varying the contrast of a single face image. We observe a monotonic variation of VAE likelihoods with image contrast: the highest likelihoods occur for the images with highest contrast (greater variance in pixel values) and likelihoods progressively decrease with image contrast (Fig. 1f). In other words, image contrasts also bias VAE likelihoods strongly.

We note that humans are able to robustly handle such variations in pixel intensity and contrast quite comfortably. In the next section, we propose remedies for outlier detection inspired by the biology of the mammalian visual system.

3 Efficient remedies for robust outlier detection with VAE likelihoods

We develop three remedies for outlier detection with VAE likelihoods. The first two remedies involve correcting for the two sources of bias discussed in the previous section, and are inspired by powerful luminance and contrast normalization properties of the mammalian visual system [2, 28]. The third remedy involves an ensemble score, inspired both by robust population coding in neural ensembles [21] and earlier studies that employed deep ensembles for outlier detection [12, 3].

3.1 Bias correction for pixel intensity

We develop a theoretically-grounded correction for VAE likelihoods. For VAEs, the marginal likelihood can be written as:

$$\log p_{\theta}(\mathbf{x}) = \log \mathbb{E}_{q_{\phi}(\mathbf{z}|\mathbf{x})} [p_{\theta}(\mathbf{x}|\mathbf{z})p(\mathbf{z})/q_{\phi}(\mathbf{z}|\mathbf{x})]$$

The “negative reconstruction error” $p_{\theta}(\mathbf{x}|\mathbf{z})$ is evaluated as the likelihood of the reconstructed input $\hat{\mathbf{x}}(\mathbf{z})$ based on the observation \mathbf{x} and some visible distribution (e.g. Bernoulli, continuous Bernoulli, Gaussian, categorical). The expectation itself is evaluated with Monte-Carlo integration.

We examine the reconstruction error term $p_{\theta}(\mathbf{x}|\mathbf{z})$, assuming perfect reconstruction of the input samples by the VAE. We denote this reconstruction error $\text{asc}p_{\text{cB}}(\mathbf{x}; \boldsymbol{\lambda}^*)$ where p_{cB} denotes the continuous Bernoulli pdf, and $\boldsymbol{\lambda}^*$ corresponds to its optimal parameters that correspond to perfect reconstruction ($\hat{\mathbf{x}} = \mathbf{x}$). We plot the negative reconstruction error for perfect reconstruction of different input samples with uniform pixel intensities, varying over the entire range (Fig. 2a, dashed

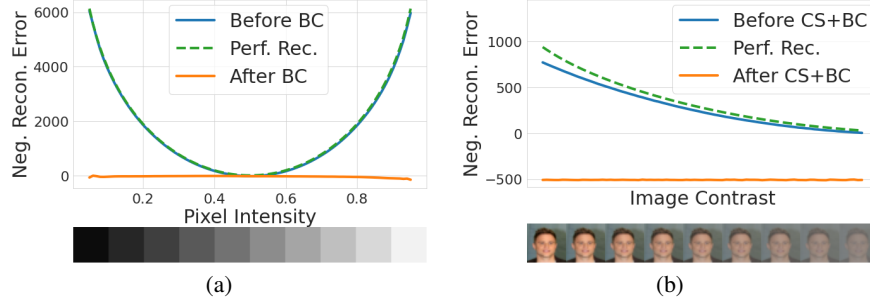


Figure 2: **Biases arising from pixel intensities and image contrasts.** (a) Negative reconstruction error for simulated images with uniform pixel intensities, ranging from full-black to full-white before (blue) and after (orange) bias correction (BC). (b) Negative reconstruction error for simulated images with varying contrasts, from highest to lowest values before (blue) and after (orange) contrast stretching (CS) and bias correction. (Both panels) Dashed green line: negative reconstruction error for perfect reconstruction with the continuous Bernoulli visible distribution.

green). $p_{cB}(\mathbf{x}; \lambda^*)$ exhibits a bias that is nearly identical with the marginal likelihood (Fig. 1c). In other words, even if two input samples are perfectly reconstructed by the VAE, these will be assigned different likelihoods, depending on the average pixel intensity in each sample; a bias that is largely driven by the reconstruction error term.

We eliminate this bias in the reconstruction error by dividing by the error for perfect reconstruction. The “bias-corrected” marginal likelihood (BC) evaluates to:

$$\log p_{\theta}^c(\mathbf{x}) = \log \mathbb{E}_{q_{\phi}(\mathbf{z}|\mathbf{x})} \left[\frac{p_{\theta}(\mathbf{x}|\mathbf{z})}{p_{cB}(\mathbf{x}; \lambda^*)} \frac{p(\mathbf{z})}{q_{\phi}(\mathbf{z}|\mathbf{x})} \right] = \log p_{\theta}(\mathbf{x}) - \log p_{cB}(\mathbf{x}; \lambda^*) \quad (1)$$

where, in the last step, $p_{cB}(\mathbf{x}; \lambda^*)$ is moved outside the expectation as it does not depend on \mathbf{z} . The exact procedure for computing the correction term for the Bernoulli and continuous Bernoulli visible distributions is shown in Appendix B. For the categorical visible distribution, an equivalent empirical correction is presented in Appendix G.

Following bias correction, the bias in the negative reconstruction error is eliminated (Fig. 2a, orange). We note that this correction is sample-specific, and can be applied *post hoc* during evaluation time; it does not require retraining the VAE.

3.2 Normalization of image contrasts

For eliminating the second source of bias arising from image contrasts, we propose a standard image pre-processing step: “contrast stretching”. Each image sample, for both training and testing data, is contrast normalized with the following transformation: $x_i = \min(\max(0, [x_i - a]/r), 1)$, where x_i refers to the i^{th} pixel of image \mathbf{x} , $r = P_{95}(\text{vec}(\mathbf{x})) - P_5(\text{vec}(\mathbf{x}))$, $a = P_5(\text{vec}(\mathbf{x}))$, P_j refers to the j^{th} percentile and $\text{vec}()$ represents the vectorization of the input sample tensor. Following contrast stretching, we observe more homogeneous distributions of per-channel variance across datasets (Appendix E.4; Fig. 9b).

Again, variation in image contrasts produces systematic biases in the negative reconstruction error (Fig. 2b, blue); this bias persists even if the negative reconstruction error was computed assuming perfect reconstruction (Fig. 2b, dashed green). Contrast stretching and bias correction significantly ameliorate this bias (Fig. 2b, orange). For subsequent experiments, VAEs were both trained and tested with contrast stretched images (Appendix A), although contrast stretching at test time alone sufficed to achieve robust outlier detection (section 4.1, ablation experiments).

3.3 Ensemble variance of likelihoods

“Deep ensembles” are among the most successful approaches for outlier detection, particularly with labeled data [12, 20]. Recently, this result has also been extended to deep generative models with unlabeled data [3]. Inspired by these previous studies and our theoretical results on biases in image likelihoods, we compute an ensemble score: the variance of the log-likelihood across multiple, independently trained VAEs: $EV = \text{Var}_{k=1}^N [\log p_{\theta}^k(\mathbf{x})]$.

We reason that since each image’s likelihood is systematically biased by the same amount across the ensemble, the variance of the likelihood estimate across the ensemble would be relatively unaffected by these biases. Specifically, we expect ensemble variance to be lower for in-distribution data than for out-of-distribution data, due to more consistent projections into the latent space, and consequently, more consistent reconstructions of the input samples. For experiments reported here, we employed 6 VAEs trained with different, random weight initializations and train-validation splits (Appendix A).

4 Experiments

We trained and tested VAEs with multiple grayscale and natural image datasets. First, we trained VAEs with four grayscale image datasets – MNIST, Fashion-MNIST, EMNIST (handwritten English letters [5]) and KMNIST (handwritten Japanese characters [4]) – and tested them against four outlier datasets each. These outlier datasets comprised each of the other three datasets (the ones that the VAE was not trained on) and a grayscale, uniform noise dataset. Next, we trained VAEs with five natural image datasets – SVHN (Street View House Numbers [19]), CelebA, ComprehensiveCars (traffic surveillance camera views of cars [31]), GTSRB (German Traffic Sign Recognition Benchmark) and CIFAR-10 [11] – and tested them against five outlier datasets each. Again, the outlier datasets comprised each of the other four datasets, and a colored, uniform noise dataset. Data source and pre-processing details are provided in Appendix C. Each VAE was trained 6 times, with 3 different random initializations of the network weights across 2 train-validation splits; we report both average performance measures across all 6 runs (e.g. Figs. 3a, 3b) and standard deviations (Appendices E.2-E.3, Tables 3 and 4).

4.1 Bias-corrected likelihoods and ensemble variance scores improve outlier detection

We compared the outlier detection performance of the vanilla (uncorrected) VAE likelihood (LL) against the bias corrected likelihood (BC-LL) and the ensemble variance of VAE likelihoods (EV-LL). Both train and test images were contrast stretched prior to computing BC-LL and EV-LL scores. Comparisons with other competing approaches are presented in the next section. We present the results as a grid (4×5 or 5×6) of area under the ROC curve (AUROC) values: higher values indicate better outlier detection (details in Appendix D). Corresponding results for area under the precision-recall curve (AUPRC) and false-positive rate at 80% true-positive rate (FPR@80%TPR) are provided in Appendices E.2-E.3 (Figs. 7a, 7b, 8a and 8b).

First, we evaluated our remedies for outlier detection with VAEs trained on grayscale image datasets. In nearly every case, we found that bias-corrected likelihoods (BC-LL, Fig. 3a, orange squares) outperformed uncorrected likelihoods (LL, Fig. 3a, blue circles); AUROC values for outlier detection approached ceiling levels, in many cases. For example, bias correction resolved the problematic case of the Fashion-MNIST VAE such that in-distribution Fashion-MNIST samples were assigned higher bias-corrected likelihoods than out-of-distribution MNIST samples (Fig. 4a), resulting in a perfect AUROC. (Fig. 4b). Moreover, samples that were assigned the highest and lowest bias-corrected likelihoods were visually more typical and atypical, respectively (Fig. 4c), as compared to those based on uncorrected likelihoods (Fig. 1b).

Across all outlier datasets tested with the Fashion-MNIST VAE, AUROC was typically at or near ceiling with the bias-corrected likelihoods (Fig. 3a, second column). On average, we observed consistent improvements in outlier detection accuracies with the bias correction across all grayscale VAEs (Fig. 3a, last row). The ensemble variance scores (EV-LL) also performed comparably with the bias-corrected likelihoods (Figure 3a, green diamonds). For the KMNIST dataset, we found improvements in all but one case: some Fashion-MNIST samples were assigned higher likelihoods, more so, after bias correction. We analyze this single failure case in Appendix F.1 and show that, even for this dataset, our remedy ameliorated likelihood bias and identified typical exemplars.

Next, we tested these remedies with VAEs trained on natural image datasets. Again, in nearly every case the BC-LL score (Fig. 3b, orange squares) outperformed uncorrected likelihoods (Fig. 3b, blue circles). For example, for the CelebA VAE, AUROC values ranged between 47-79 with the uncorrected likelihoods (across all out-of-distribution datasets, except Noise), whereas these values improved to 85-88 with bias correction (Fig. 3b, second column, Fig. 4d, and Fig 4e). Similarly, with ensemble variance, AUROC values improved to 81-91 across test datasets (Fig. 3b, second column, green diamonds). Moreover, CelebA samples assigned the highest and lowest bias-corrected likelihoods were visually more typical: the highest likelihood samples contained face images on

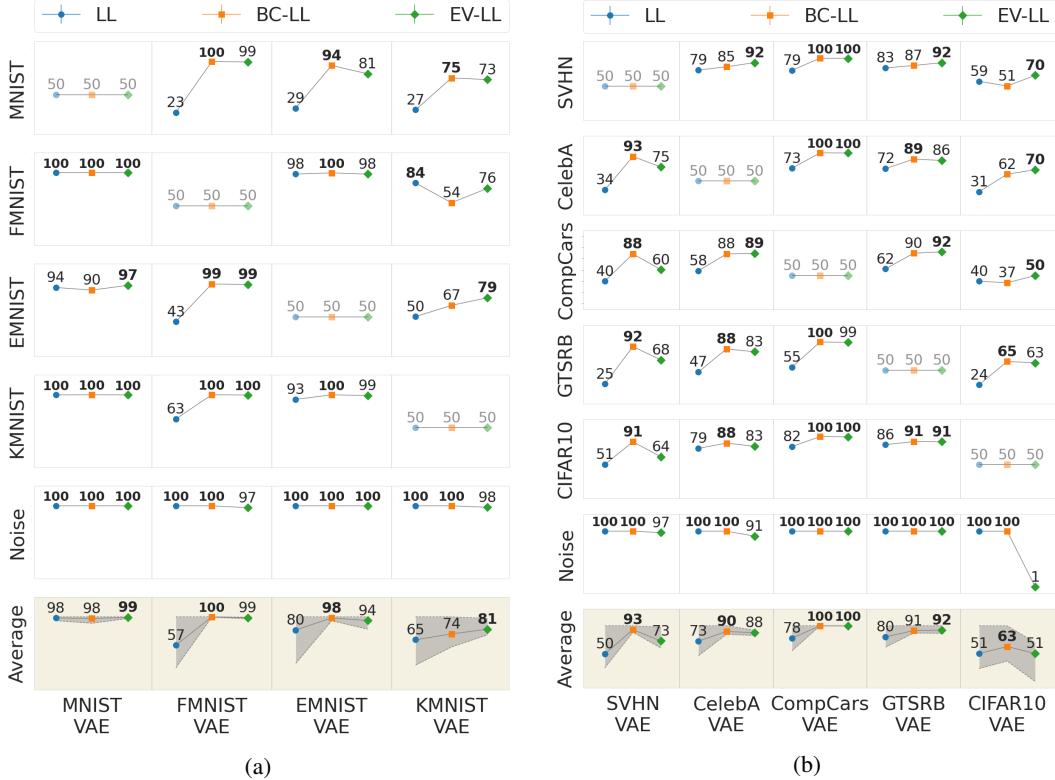


Figure 3: **Outlier detection with bias corrected likelihoods and ensemble variance.** (a) Outlier detection AUROC values for VAEs trained with grayscale image datasets and tested with other grayscale datasets (or noise). Each column represents a training dataset, and each row represents a test dataset. Last row: average AUROC across all test datasets for each VAE. Blue, orange and green symbols: AUROC with uncorrected log likelihoods (LL), bias-corrected log likelihoods (BC-LL), and ensemble variance of log likelihoods (EV-LL), respectively. Higher values indicate better outlier detection performance. Numbers in **bold** indicate highest AUROC values across the three scores for each train-test combination. Gray shading in the last row: minimum and maximum values for each score across test datasets. (b) Same as in (a) but for VAEs trained with natural image datasets and tested with other natural image datasets (or noise).

typical plain backgrounds, whereas the lowest likelihood samples comprised of face images with extraneous objects, such as headgear, unconventional attire or unusual backgrounds (Fig. 4f).

Ablation experiments revealed the relative contributions of contrast stretching and bias correction. Contrast stretching was essential to achieving high accuracies, particularly with the natural image datasets (Appendix E.4, Fig. 10, brown symbols). In fact, contrast stretching of the test samples alone sufficed to achieve robust outlier detection: Even with a VAE trained on the original images (without contrast stretching), outlier detection accuracies improved if contrast stretching was applied at test time alone (Fig. 10, pink symbols). Finally, contrast normalization with techniques other than contrast stretching (e.g. histogram equalization) also yielded comparable outlier detection accuracies (Fig. 10, magenta symbols).

We repeated these analyses for a VAE with a categorical visible distribution (Appendix G). Again, we observed marked improvements in outlier detection performance with bias-corrected likelihoods. Overall, these results confirm the effectiveness of our remedies for outlier detection with VAE likelihoods across multiple grayscale and natural image datasets, and different VAE visible distributions.

4.2 Comparison with state-of-the-art outlier detection methods

We compared accuracies with the bias-corrected likelihood (BC-LL) and ensemble variance (EV-LL) scores against four competing, state-of-the-art approaches: i) input complexity (IC), ii) likelihood ratio (LRat), iii) likelihood regret (LReg) and iv) WAIC (Watanabe-Akaike Information Criterion). Briefly,

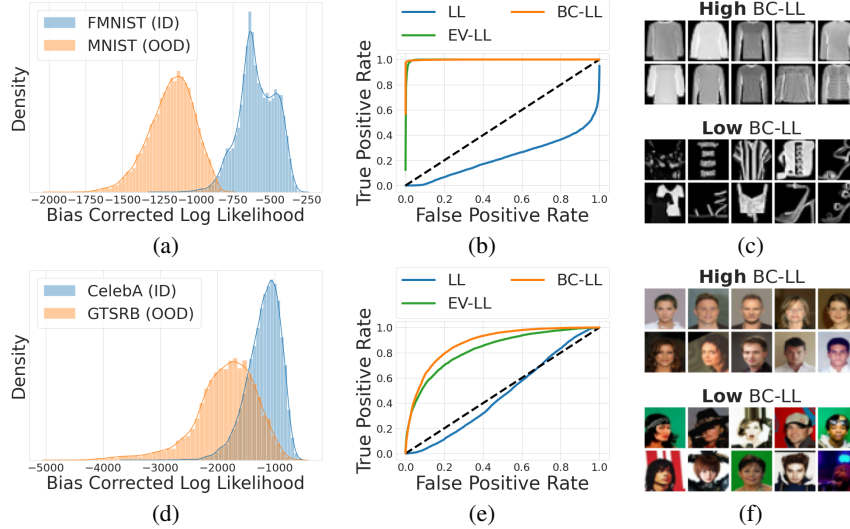


Figure 4: **Bias correction improves outlier detection.** (a) Same as in Figure 1a but showing bias-corrected log-likelihoods for the Fashion-MNIST VAE. (b) AUROC curves for outlier detection with Fashion-MNIST VAE likelihoods using MNIST (OOD) test samples without (blue) bias correction, with bias correction (orange) or with the ensemble variance score (green). (c) Same as in Figure 1b but showing Fashion-MNIST samples with highest (top row) and lowest (bottom row) likelihoods following bias correction. **d-f** Same as in panels a-c, but showing results for the CelebA VAE, with out-of-distribution GTSRB samples, following bias correction.

IC employs a subtractive bias correction for each sample; the correction is computed based on sample complexity estimated with one of many compression algorithms (e.g. JPEG) [25]. The likelihood ratio score computes the ratio between the sample likelihood obtained with a VAE trained with the original data, and one trained with noise-corrupted images [23]. Likelihood regret computes the improvement in the log-likelihood for a particular sample that can be achieved with a sample-specific optimization of the posterior $q_\phi(\mathbf{z}|\mathbf{x})$ [30]. Finally, WAIC is computed as $\mathbb{E}_\theta[\log p_\theta(\mathbf{x})] - \text{Var}_\theta[\log p_\theta(\mathbf{x})]$, from an ensemble of deep generative models [3] (Appendix D, for details).

First, we performed an exhaustive (4×5) comparison of approaches with grayscale VAEs and datasets. For illustration, we discuss results for the problematic Fashion-MNIST VAE (Fig. 5a, top row); the full set of comparisons is presented in Appendix E.5 (Fig. 11). Both BC-LL scores and EV-LL outperformed, or performed comparably with, other state-of-the-art methods for detecting outliers with the Fashion-MNIST VAE (Figure 5a, top row). Interestingly, IC performed relatively poorly for this VAE (Fig. 5a, top row, violet symbols). Similar results were observed with the other grayscale VAEs: on average, BC-LL and EV-LL AUROC values were comparable with state-of-the-art approaches (Figure 5a, second row, Average). A notable exception was the KMNIST dataset for which outlier detection with BC-LL and EV-LL scores was sub-par (Fig. 5a, bottom row, last column). Interestingly, other outlier detection approaches (except IC) also fared comparatively poorly with this dataset.

Next, we performed an exhaustive (5×6) comparison of all approaches with natural image VAEs and datasets. Again, we illustrate the results with the CelebA VAE (Fig. 5b); the full set of comparisons is presented in Appendix E.5 (Fig. 12). As before, we noticed superlative outlier detection performance with the BC-LL and EV-LL scores (Fig. 5b, top row). Although, other methods (e.g. IC or LReg) performed better at detecting outliers belonging to specific datasets (e.g. SVHN, Figure 5b, top row, first column), the BC-LL and EV-LL scores yielded the highest average AUROC values across all outlier datasets tested with the CelebA VAE (Figure 5b, bottom row, second column). Overall, across all combinations of VAEs and outlier datasets tested, BC-LL and EV-LL scores performed more consistently and yielded AUROC values on par with, or exceeding, state-of-the-art (Figure 5b, bottom row). Interestingly, outlier detection with BC-LL and EV-LL, as well as with the other scores, was relatively poor for the CIFAR-10 dataset comprised of heterogeneous object categories; this case is discussed further in Appendix F.2.

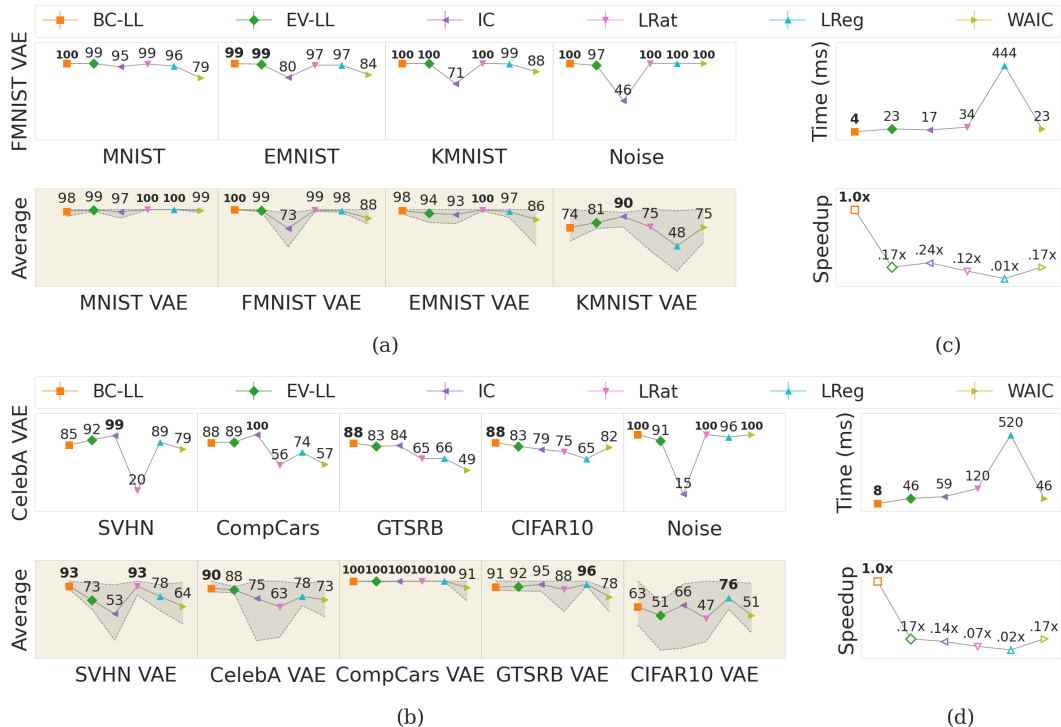


Figure 5: **Comparison with four competing outlier detection approaches** (IC: input complexity; LRat: Likelihood Ratio; LReg: Likelihood Regret; WAIC: Watanabe Akaike Information Criterion). (a) (Top row) AUROC values with the different outlier detection methods for a VAE trained with the Fashion-MNIST dataset. Each column represents a different outlier dataset. (Bottom row) Same as in top row but showing average outlier detection AUROC for 4 different grayscale image VAEs (columns), each tested with the other 3 grayscale image datasets and noise. Gray shading: AUROC range across test datasets. (b) (Top row) Same as in (a, top row) but showing AUROC values for a VAE trained with the CelebA dataset. (Bottom row) Same as in (a, bottom row) but showing average outlier detection AUROC for 5 different natural image VAEs (columns), each tested with the other 4 natural image datasets and noise (see also Appendix E.5, Figs. 11, 12). (c) (Top) Compute times (ms) for evaluating 500 test samples with each approach, for a grayscale image VAE (lower is better). (Bottom) Speedup factor computed as the ratio of the compute time for each approach to the compute time for the BC-LL score (higher is better). (d) Same as in (c), but for a natural image VAE.

Finally, we compared compute times for our scores with previous outlier detection approaches (average inference time for evaluating 500 samples from each test dataset). Again, compute times for our scores were comparable with or outperformed competing approaches by a factor of up to 100x (Figure 5c-d), for both grayscale and natural image datasets (details in Appendix E.6).

5 Related work

Our work is inspired by previous studies that seek to correct for biases in generative model likelihoods. Our bias correction is, perhaps, most closely related to the work of Serra et al. (2019) [25] who proposed a correction for Glow and PixelCNN++ model likelihoods based on “input complexity” (IC). Their out-of-distribution score is computed by subtracting a sample-specific complexity estimate $L(\mathbf{x})$ from the negative log-likelihood (compare with our Equation (1)). Nonetheless, IC depends on the particular choice of a compression algorithm (e.g. PNG, JPEG2000, FLIF), which is unrelated to the VAE, whereas our correction is theoretically-grounded and contingent on the VAE decoder visible distribution. Interestingly, IC’s outlier detection performance is sub-par for the Fashion-MNIST VAE (Fig. 5a, top row), and it also fails to distinguish in-distribution data from uniform noise for several natural image datasets (Appendix E.5, Fig. 12, sixth row).

Ren et al. (2019) [23] originally highlighted the problem of bias in deep generative model likelihoods, for samples with many zero-valued pixels. They proposed correcting for this bias by training a second

generative model with noise-corrupted samples to capture background statistics; the “likelihood ratio” between the original and noisy VAEs provided a sensitive readout of foreground object statistics. With VAEs, our bias correction matches or outperforms the likelihood ratio score, on average (Figures 5a-b, bottom rows). Our bias correction also obviates the need for training multiple, duplicate models.

Similarly, Nalisnick et al. (2019) [18] originally identified the problem of bias in likelihoods arising from sample variance, and proposed a typicality test for robust outlier detection [17]. However, the typicality test works best with batches of samples, and performs relatively poorly with single samples. Interestingly, with the continuous Bernoulli visible distribution, our likelihood trends are opposite to those reported by Nalisnick et al. [18]: Samples with the lowest contrasts yield the lowest likelihoods, and vice versa, (Fig. 1f), indicating that biases with VAE likelihoods depend on the choice of visible distribution (see Appendix G for a detailed discussion).

Our ensemble variance score is inspired by previous studies that demonstrated the effectiveness of deep ensembles for outlier detection (e.g. [3, 12]). Nonetheless, many of these approaches (e.g. [12, 14]) do not work with unlabeled data. A notable exception is the WAIC score proposed by Choi et al. (2018) [3]. However, the WAIC score lacks clear theoretical arguments for its efficacy [17]. Our EV-LL score outperforms the WAIC score, on average (Figures 5a-b, bottom rows).

Recent work by Yong et al. (2020) [32] proposed employing bias-free Gaussian likelihoods and their variances for outlier detection. Yet, Gaussian visible distributions are not theoretically appropriate to model the finite range of pixel values (0-255) encountered in images. One way of overcoming this challenge is to discretize the Gaussian (or logistic) visible distribution with an underlying categorical representation, a solution adopted by other studies (e.g. PixelCNN++ [24]). However, in practice, such a categorical distribution also concentrates probability mass at the edges (0 and 255 values), yielding systematically biased likelihoods (Appendix G). Moreover, Yong et al.’s approach does not work well with natural image datasets (their Appendix C). Our contrast normalization and bias correction enables robust outlier detection, even with natural image datasets.

Xiao et al. (2020) [30] proposed a “likelihood regret” metric that involves quantifying the improvement in marginal likelihood by retraining the encoder network to obtain optimal likelihood for each sample. Such sample-specific optimizations are computationally expensive, for example, when millions of samples need to be evaluated on-the-fly. In contrast, our proposed metrics are readily computed with a single forward pass through pre-trained VAEs, leading to a 50-100x speedup in evaluation times over likelihood regret (e.g. Fig. 5c-d). Interestingly, Xiao et al also showed that other state-of-the-art outlier detection metrics (e.g. IC, likelihood ratios) perform comparatively poorly with VAEs.

6 Conclusions and Societal Implications

We have proposed, and extensively tested, three simple and efficient remedies to achieve robust outlier detection with VAE likelihoods. Our remedies – for correcting the bias induced by average pixel intensities and contrasts – are inspired by well-known luminance and contrast normalization properties of the mammalian visual system [2]. We demonstrate the effectiveness of these remedies for outlier detection with multiple grayscale and natural image datasets (total of 9 datasets), and two different, popular VAE visible distributions (continuous Bernoulli and categorical). In all cases, our remedies achieve or outperform four other state-of-the-art, competing approaches [25, 23, 30, 3]. In addition, our remedies are computationally inexpensive and significantly outperform all competing approaches in terms of evaluation times. Taken together, these results indicate that our theoretically-grounded remedies suffice to ameliorate biases arising from low-level image statistics, and achieve robust outlier detection with VAE likelihoods.

The fact that VAE (and other deep generative model) likelihoods can be biased by low-level image statistics could be exploited by adversarial algorithms to disguise outliers as inliers or vice versa. While our remedies mitigate this shortcoming, we note that certain types of datasets pose a challenge for outlier detection with VAEs. For example, all VAE-based approaches tested here fail to achieve superlative outlier detection with the VAE trained on the CIFAR-10 dataset (Fig. 5b, bottom row, last column). Even with our remedies, the best outlier detection occurs, by far, for datasets with relatively homogeneous images in which the objects of interest appear at consistent spatial locations relative to the bounding frame (edge) of the image (e.g. CompCars, GTSRB). We examine the reasons for this failure, and explore fundamental limitations for outlier detection with VAEs, and their implications, in Appendix F.2.

Nonetheless, the remedies we propose for VAEs also have positive implications for key real-world applications. For example, medical imaging data such as retinal scans or MRI images are typically acquired in highly stereotyped spatial coordinates. In such cases, VAEs can be deployed as expert deep learning systems that exploit the spatial consistency of image features for fine-grained outlier detection (e.g. pathological conditions). Future work will explore these applications.

References

- [1] Bidart, R. and Wong, A. (2019). Affine Variational Autoencoders: An Efficient Approach for Improving Generalization and Robustness to Distribution Shift. *arXiv e-prints*, page arXiv:1905.05300.
- [2] Carandini, M., Demb, J. B., Mante, V., Tolhurst, D. J., Dan, Y., Olshausen, B. A., Gallant, J. L., and Rust, N. C. (2005). Do we know what the early visual system does? *Journal of Neuroscience*, **25**(46), 10577–10597.
- [3] Choi, H., Jang, E., and Alemi, A. A. (2018). WAIC, but Why? Generative Ensembles for Robust Anomaly Detection. *arXiv e-prints*, page arXiv:1810.01392.
- [4] Clanuwat, T., Bober-Irizar, M., Kitamoto, A., Lamb, A., Yamamoto, K., and Ha, D. (2018). Deep learning for classical japanese literature. *NeurIPS Workshop on Machine Learning for Creativity and Design*.
- [5] Cohen, G., Afshar, S., Tapson, J., and van Schaik, A. (2017). EMNIST: Extending MNIST to handwritten letters. In *2017 International Joint Conference on Neural Networks (IJCNN)*, pages 2921–2926.
- [6] Hendrycks, D. and Dietterich, T. G. (2019). Benchmarking neural network robustness to common corruptions and perturbations. In *7th International Conference on Learning Representations, ICLR 2019, New Orleans, LA, USA, May 6-9, 2019*. OpenReview.net.
- [7] Kingma, D. P. and Ba, J. (2015). Adam: A method for stochastic optimization. In Y. Bengio and Y. LeCun, editors, *3rd International Conference on Learning Representations, ICLR 2015, San Diego, CA, USA, May 7-9, 2015, Conference Track Proceedings*.
- [8] Kingma, D. P. and Dhariwal, P. (2018). Glow: Generative flow with invertible 1x1 convolutions. In S. Bengio, H. Wallach, H. Larochelle, K. Grauman, N. Cesa-Bianchi, and R. Garnett, editors, *Advances in Neural Information Processing Systems*, volume 31. Curran Associates, Inc.
- [9] Kingma, D. P. and Welling, M. (2014). Auto-encoding variational bayes. In Y. Bengio and Y. LeCun, editors, *2nd International Conference on Learning Representations, ICLR 2014, Banff, AB, Canada, April 14-16, 2014, Conference Track Proceedings*.
- [10] Kirichenko, P., Izmailov, P., and Wilson, A. G. (2020). Why normalizing flows fail to detect out-of-distribution data. In H. Larochelle, M. Ranzato, R. Hadsell, M. F. Balcan, and H. Lin, editors, *Advances in Neural Information Processing Systems*, volume 33, pages 20578–20589. Curran Associates, Inc.
- [11] Krizhevsky, A. (2009). Learning multiple layers of features from tiny images. Technical report, University of Toronto.
- [12] Lakshminarayanan, B., Pritzel, A., and Blundell, C. (2017). Simple and scalable predictive uncertainty estimation using deep ensembles. In I. Guyon, U. V. Luxburg, S. Bengio, H. Wallach, R. Fergus, S. Vishwanathan, and R. Garnett, editors, *Advances in Neural Information Processing Systems*, volume 30. Curran Associates, Inc.
- [13] LeCun, Y. and Cortes, C. (2010). MNIST handwritten digit database.
- [14] Liang, S., Li, Y., and Srikant, R. (2018). Enhancing the reliability of out-of-distribution image detection in neural networks. In *6th International Conference on Learning Representations, ICLR 2018, Vancouver, BC, Canada, April 30 - May 3, 2018, Conference Track Proceedings*. OpenReview.net.
- [15] Liu, Z., Luo, P., Wang, X., and Tang, X. (2015). Deep learning face attributes in the wild. In *2015 IEEE International Conference on Computer Vision (ICCV)*, pages 3730–3738.
- [16] Loaiza-Ganem, G. and Cunningham, J. P. (2019). The continuous bernoulli: fixing a pervasive error in variational autoencoders. In H. Wallach, H. Larochelle, A. Beygelzimer, F. d'Alché-Buc, E. Fox, and R. Garnett, editors, *Advances in Neural Information Processing Systems*, volume 32. Curran Associates, Inc.

- [17] Nalisnick, E., Matsukawa, A., Whye Teh, Y., and Lakshminarayanan, B. (2019). Detecting Out-of-Distribution Inputs to Deep Generative Models Using Typicality. *arXiv e-prints*, page arXiv:1906.02994.
- [18] Nalisnick, E. T., Matsukawa, A., Teh, Y. W., Görür, D., and Lakshminarayanan, B. (2019). Do deep generative models know what they don't know? In *7th International Conference on Learning Representations, ICLR 2019, New Orleans, LA, USA, May 6-9, 2019*. OpenReview.net.
- [19] Netzer, Y., Wang, T., Coates, A., Bissacco, A., Wu, B., and Ng, A. Y. (2011). Reading digits in natural images with unsupervised feature learning. *NeurIPS workshop on Deep Learning and Unsupervised Feature Learning*.
- [20] Ovadia, Y., Fertig, E., Ren, J., Nado, Z., Sculley, D., Nowozin, S., Dillon, J., Lakshminarayanan, B., and Snoek, J. (2019). Can you trust your model's uncertainty? evaluating predictive uncertainty under dataset shift. In H. Wallach, H. Larochelle, A. Beygelzimer, F. d'Alché-Buc, E. Fox, and R. Garnett, editors, *Advances in Neural Information Processing Systems*, volume 32. Curran Associates, Inc.
- [21] Pouget, A., Dayan, P., and Zemel, R. (2000). Information processing with population codes. *Nature Reviews Neuroscience*, **1**(2), 125–132.
- [22] Radford, A., Metz, L., and Chintala, S. (2016). Unsupervised representation learning with deep convolutional generative adversarial networks. In Y. Bengio and Y. LeCun, editors, *4th International Conference on Learning Representations, ICLR 2016, San Juan, Puerto Rico, May 2-4, 2016, Conference Track Proceedings*.
- [23] Ren, J., Liu, P. J., Fertig, E., Snoek, J., Poplin, R., Depristo, M., Dillon, J., and Lakshminarayanan, B. (2019). Likelihood ratios for out-of-distribution detection. In H. Wallach, H. Larochelle, A. Beygelzimer, F. d'Alché-Buc, E. Fox, and R. Garnett, editors, *Advances in Neural Information Processing Systems*, volume 32. Curran Associates, Inc.
- [24] Salimans, T., Karpathy, A., Chen, X., and Kingma, D. P. (2017). Pixelcnn++: Improving the pixelcnn with discretized logistic mixture likelihood and other modifications. In *5th International Conference on Learning Representations, ICLR 2017, Toulon, France, April 24-26, 2017, Conference Track Proceedings*. OpenReview.net.
- [25] Serrà, J., Álvarez, D., Gómez, V., Slizovskaia, O., Núñez, J. F., and Luque, J. (2020). Input complexity and out-of-distribution detection with likelihood-based generative models. In *8th International Conference on Learning Representations, ICLR 2020, Addis Ababa, Ethiopia, April 26-30, 2020*. OpenReview.net.
- [26] Snoek, J., Larochelle, H., and Adams, R. P. (2012). Practical bayesian optimization of machine learning algorithms. In F. Pereira, C. J. C. Burges, L. Bottou, and K. Q. Weinberger, editors, *Advances in Neural Information Processing Systems*, volume 25. Curran Associates, Inc.
- [27] Stallkamp, J., Schlipsing, M., Salmen, J., and Igel, C. (2012). Man vs. computer: Benchmarking machine learning algorithms for traffic sign recognition. *Neural Networks*, **32**, 323–332. Selected Papers from IJCNN 2011.
- [28] Stockman, A., Langendörfer, M., Smithson, H. E., and Sharpe, L. T. (2006). Human cone light adaptation: From behavioral measurements to molecular mechanisms. *Journal of Vision*, **6**(11), 5–5.
- [29] Xiao, H., Rasul, K., and Vollgraf, R. (2017). Fashion-MNIST: a novel image dataset for benchmarking machine learning algorithms.
- [30] Xiao, Z., Yan, Q., and Amit, Y. (2020). Likelihood regret: An out-of-distribution detection score for variational auto-encoder. In H. Larochelle, M. Ranzato, R. Hadsell, M. F. Balcan, and H. Lin, editors, *Advances in Neural Information Processing Systems*, volume 33, pages 20685–20696. Curran Associates, Inc.
- [31] Yang, L., Luo, P., Loy, C. C., and Tang, X. (2015). A large-scale car dataset for fine-grained categorization and verification. In *2015 IEEE Conference on Computer Vision and Pattern Recognition (CVPR)*, pages 3973–3981.

- [32] Yong, B. X., Pearce, T., and Brintrup, A. M. (2020). Bayesian autoencoders : Analysing and fixing the bernoulli likelihood for out-of-distribution detection. *ICML Workshop on Uncertainty & Robustness in Deep Learning*.

Supplementary Material: Appendices

Appendix A: VAE architecture and training

All experiments were performed using Tensorflow 2 and Tensorflow Probability libraries. We employed a convolutional VAE architecture that follows the DCGAN [22] structure (Table 1), nearly identical with that of [30]. We used the Adam optimizer [7] with a learning rate of 5e-4 for training all of our models. Each model was trained for 1000 epochs with a batch size of 64, and the checkpoint with best validation performance based on negative log-likelihood was used for reporting results. We used the Xavier uniform initializer (default in Tensorflow 2) for initializing network weights.

For reporting results based on the bias-corrected log-likelihood (BC-LL score) we used a VAE with a latent dimension (nz) of size 20. To examine the robustness of our remedies to VAE architecture, we also trained four additional VAEs with latent dimensions of size 40, 60, 80, and 100 (see Appendix E.1, Figure 6). For reporting results with Ensemble Variance (EV-LL score), we computed variance of the bias corrected log likelihoods across six runs of the default VAE (nz=20; see section 4, Experiments); in-distribution data is expected to have lower EV-LL than out-of-distribution data. The same architecture was used for training both grayscale and natural image VAEs, with two differences (grayscale: nf = 32, nc = 1; natural: nf = 64, nc = 3). Log likelihoods were estimated using the importance weighted lower bound (n=100 samples) [30].

Table 1: VAE architecture. nc: number of channels; nf: number of filters; nz: number of latent dimensions; BN: batch normalization; Conv: convolution layer; DeConv: deconvolution layer; ReLU: rectified linear unit

Encoder	Decoder
Input image of shape $32 \times 32 \times \text{nc}$	Input latent code, reshape to $1 \times 1 \times \text{nz}$
4×4 Conv _{nf} Stride=2, BN, ReLU	4×4 DeConv _{4 × nf} Stride=1, BN, ReLU
4×4 Conv _{2 × nf} Stride=2, BN, ReLU	4×4 DeConv _{2 × nf} Stride=2, BN, ReLU
4×4 Conv _{4 × nf} Stride=2, BN, ReLU	4×4 DeConv _{nf} Stride=2, BN, ReLU
4×4 Conv _{2 × nz} Stride=1	4×4 DeConv _{nc} Stride=2

Appendix B: Bias correction for Bernoulli and continuous Bernoulli decoders

Bias correction for the Bernoulli decoder. For a VAE decoder with a Bernoulli visible distribution, the negative reconstruction error is given by:

$$\begin{aligned} \log p_{\theta}(\mathbf{x}|\mathbf{z}) &= \log p_{\text{B}}(\mathbf{x}; \hat{\mathbf{x}}_{\theta}(\mathbf{z})) \\ &= \sum_{i=1}^D x_i \log \hat{x}_i + (1 - x_i) \log(1 - \hat{x}_i) \end{aligned}$$

where x_i is the pixel value of the i^{th} pixel in the input sample and \hat{x}_i (or $\hat{x}_i(\mathbf{z})$) is the corresponding pixel value in the image reconstructed by the decoder, and \mathbf{z} is the latent representation corresponding to the input image (see [9] their Appendix C.1).

The negative reconstruction error for perfect reconstruction is simply calculated by setting $\hat{x}_i = x_i$, as:

$$\log p_{\text{B}}(\mathbf{x}; \mathbf{x}) = \sum_{i=1}^D x_i \log x_i + (1 - x_i) \log(1 - x_i)$$

Bias correction for the continuous Bernoulli decoder. For a VAE decoder with a continuous Bernoulli visible distribution, the negative reconstruction error is given by:

$$\begin{aligned} \log p_{\theta}(\mathbf{x}|\mathbf{z}) &= \log p_{\text{cB}}(\mathbf{x}; \boldsymbol{\lambda}_{\theta}(\mathbf{z})) \\ &= \sum_{i=1}^D \log C(\lambda_i) + x_i \log \lambda_i + (1 - x_i) \log(1 - \lambda_i) \end{aligned} \quad (2)$$

Note that the continuous Bernoulli decoder outputs the shape parameter (λ_i) for the i^{th} pixel. The decoded pixel value itself is given by:

$$\hat{x}_i = \frac{\lambda_i}{2\lambda_i - 1} + \frac{1}{2 \tanh^{-1}(1 - 2\lambda_i)} \quad \text{if } \lambda_i \neq \frac{1}{2}$$

$$= \frac{1}{2} \quad \text{if } \lambda_i = \frac{1}{2}$$

As before, for perfect reconstruction we set $\hat{x}_i = x_i$. To find the optimal λ_i^* corresponding to perfect reconstruction, we used SciPy’s implementation of Nelder-Mead simplex algorithm to iteratively maximize $\log p_{\text{CB}}(x_i; \lambda_i)$; the correction was then calculated by setting $\lambda_i = \lambda_i^*$ in equation (2) above.

Appendix C: Data sources and pre-processing

Data sources. We used Tensorflow Datasets¹ for all datasets except CompCars and GTSRB. We fetched the CompCars² surveillance-nature images and GTSRB³ datasets from their respective official sources. For the EMNIST dataset, we selected only the “Letters” split. To generate noise patches, we used uniform random noise in range [0, 1], sampled independently across pixels and channels.

Data pre-processing and splits For both grayscale and natural image datasets, we resized all images to 32×32 pixels before VAE training and evaluation. For natural image datasets, we employed the cropped versions of SVHN and CelebA (default option in Tensorflow Datasets), such that the central object (numbers or faces, respectively) were approximately centered in each image. In addition, for experiments with natural image data, we preprocessed images by “contrast stretching”, where specified, with the method described in Section 3.2. For all datasets, we reserved 10% for the training data for validation (generated twice, independently). Evaluation was performed with the test splits of each dataset, as indicated in their respective sources. The specific datasets and the number of training and testing samples, and representative exemplars are shown in Table 2.

Appendix D: Performance metrics and competing methods

Computing performance metrics. We computed three performance metrics for outlier detection [23]: i) area under the receiver-operating-characteristic (AUROC), which represents the area under the curve obtained by plotting the true-positive rate versus the false-positive rate; ii) area under the precision-recall curve (AUPRC), which similarly represents the area under the curve obtained by plotting the precision versus the recall values, and iii) the false-positive rate at 80% true positive rate (FPR@80%TPR). Higher values of the first two metrics indicate better outlier detection, and vice versa for the third metric. All metrics were computed with the *scikit-learn* library.

For Figures 3a and 3b, as well as supplementary results reported in Appendix E, we computed these metrics with an all-versus-all comparison, by comparing each score distribution (e.g. BC-LL, EV-LL) for the test split of the inlier dataset against the respective score distribution for the test split of the outlier dataset (test versus test).

Implementing competing methods. For implementing competing methods, we used the same VAE architecture as in our paper, except that the number of hidden dimensions was set to 100 to match the likelihood regret paper [30]. Other details are specified below.


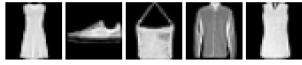



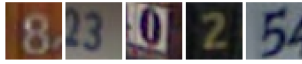





- *Input complexity (IC).* We computed input complexity by subtracting from the vanilla (uncorrected) log likelihood the “complexity” estimate $L(\mathbf{x})$ for each sample computed as $|C(\mathbf{x})|/d$, where the string of bits $C(\mathbf{x})$ was obtained with the PNG compressor (d is the dimensionality of \mathbf{x}). Log likelihoods were computed with a categorical visible distribution.

¹<https://www.tensorflow.org/datasets>

²http://mmlab.ie.cuhk.edu.hk/datasets/comp_cars/

³https://benchmark.ini.rub.de/gtsrb_dataset.html

Table 2: Details of datasets used for outlier detection with VAE likelihoods.

Dataset	Type	Exemplars	N-train (N-val)	N-test
MNIST	Grayscale		54000 (6000)	10000
Fashion-MNIST	Grayscale		54000 (6000)	10000
EMNIST-Letters	Grayscale		79920 (8880)	14800
KMNIST	Grayscale		54000 (6000)	10000
Gray-Noise	Grayscale		-	10000
SVHN	Color		65932 (7325)	26032
CelebA	Color		146493 (16277)	19962
CompCars	Color		28034 (3114)	13333
GTSRB	Color		35289 (3920)	12630
CIFAR-10	Color		45000 (5000)	10000
Color-Noise	Color		-	10000

- *Likelihood ratio (LRat)*. We trained a standard VAE and a background model using the noise-corruption procedure described in [23] with the mutation factor set to $\mu = 0.3$ for Fashion-MNIST and $\mu = 0.2$ for CelebA. We also applied a large weight decay ($\lambda = 10$), as suggested by the authors. Log likelihoods were computed with a categorical visible distribution, as in the original study.
- *Likelihood regret (LReg)*. We computed the likelihood regret score by quantifying the improvement in the likelihood for each sample by retraining the encoder for 100 epochs using the implementation provided by the authors [30]. Log likelihoods were computed with a categorical visible distribution, as in the original study.
- *Watanabe-Akaike Information Criterion (WAIC)*. WAIC was computed with the formula $\mathbb{E}_\theta[\log p_\theta(\mathbf{x})] - \text{Var}_\theta[\log p_\theta(\mathbf{x})]$, using the average log likelihood and variance across the ensemble of six VAEs (same as those employed for computing the EV-LL score). Log likelihoods were computed with a continuous Bernoulli visible distribution; the original study [3] used a Bernoulli visible distribution.

For Figures 11 and 12 that compare the performance of these other scores with our scores, AUROC values were computed by comparing each score distribution for the test split of the inlier dataset against the score distribution for test split of the outlier dataset (test versus test).

Appendix E: Supplementary results on outlier detection

E.1 Outlier detection performance with varying numbers of VAE latent dimensions

We computed outlier detection AUROC for VAEs trained with different numbers of latent dimensions (n_z). AUROC values remained more or less constant, or declined marginally with n_z (Fig. 6, blue). In addition, in all cases bias correction improved AUROC values (Fig. 6, orange versus blue).

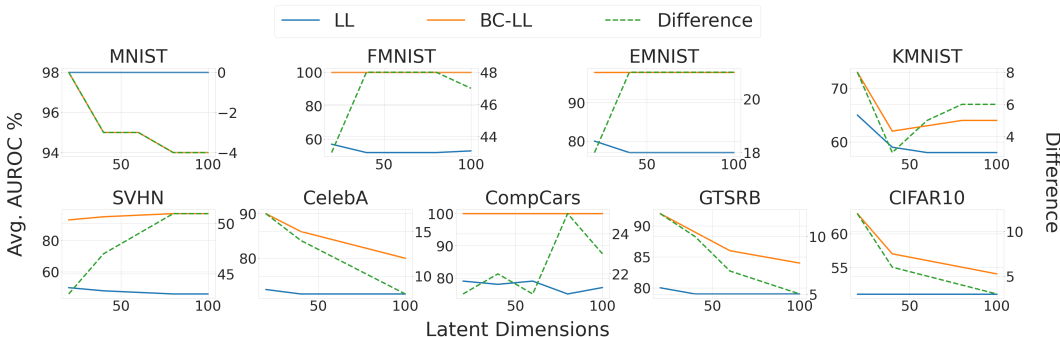


Figure 6: (*Top row*) AUROC variation with the number of latent dimensions for the four grayscale image VAEs, based on uncorrected log likelihoods (blue), bias-corrected log likelihoods (orange) and their difference (dashed green). AUROC values were averaged across all ($n=4$) outlier test datasets. (*Bottom row*) Same as in the top panel, but for five natural image VAEs, with AUROC values averaged across $n=5$ outlier datasets.

E.2 Grayscale image datasets: Additional performance metrics

In addition to AUROC (Fig. 3a), we computed AUPRC and FPR at 80% TPR for outlier detection with the grayscale VAEs, with the bias corrected likelihoods (BC-LL) and ensemble variance (EV-LL) scores. AUPRC typically improved (Fig. 7a) and FPR decreased (Fig. 7b) for the BC-LL and EV-LL scores (orange and green symbols, respectively) compared to uncorrected likelihoods (blue symbols); the KMNIST VAE tested against Fashion-MNIST outliers was the single case where our remedies failed to produce improvements. Furthermore, for the AUROC values reported in (Fig. 3a) we also report mean and standard deviation across 6 runs (3 random weight initializations \times 2 train-validation splits) in Table 3.

Table 3: BC-LL AUROC values for VAEs trained with grayscale image datasets. Columns indicate training datasets (ID) and rows indicate test datasets (OOD).

MNIST	50.0 ± 0.0	99.89 ± 0.01	94.06 ± 0.18	75.15 ± 1.34
FMNIST	99.98 ± 0.0	50.0 ± 0.0	99.6 ± 0.03	54.45 ± 2.25
EMNIST	90.31 ± 0.27	99.49 ± 0.03	50.0 ± 0.0	67.25 ± 1.44
KMNIST	100.0 ± 0.0	99.99 ± 0.0	99.89 ± 0.01	50.0 ± 0.0
Noise	100.0 ± 0.0	99.99 ± 0.0	100.0 ± 0.0	99.97 ± 0.02
OOD $\uparrow \setminus$ ID \rightarrow	MNIST	FMNIST	EMNIST	KMNIST

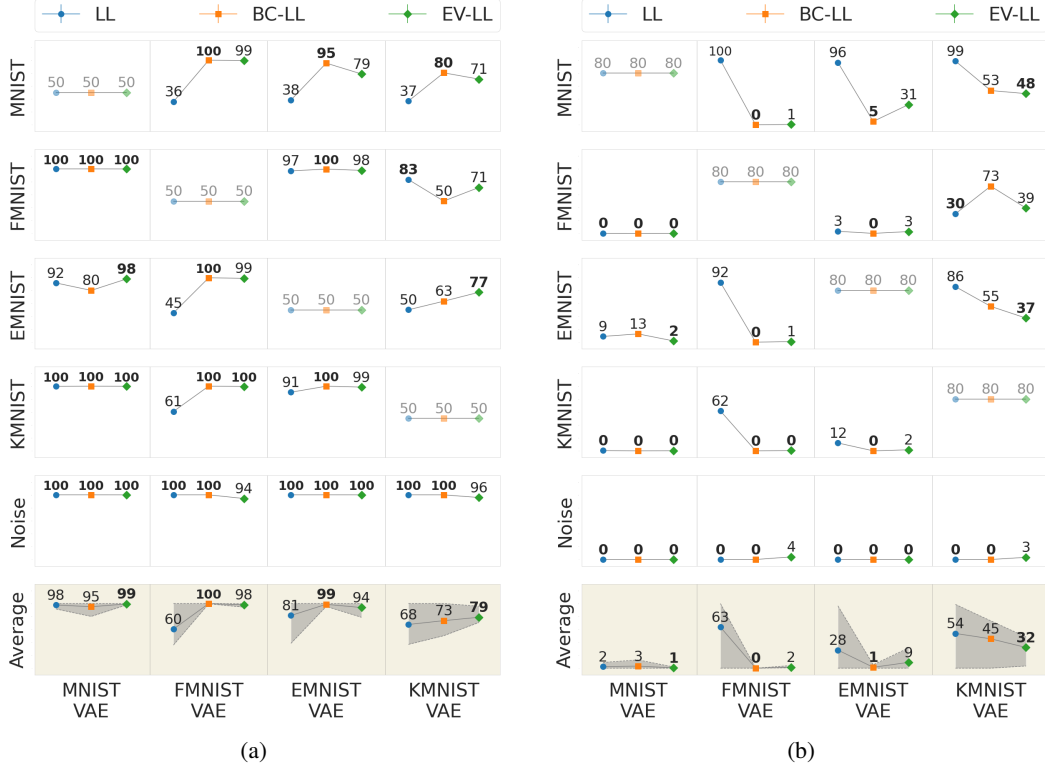


Figure 7: Additional metrics for outlier detection based on grayscale image VAE likelihoods. **(a)** Area under the precision recall curve (AUPRC) (higher is better). **(b)** False-positive rate (FPR) at a true-positive rate (TPR) of 80% (lower is better). Other conventions are the same as in Fig. 3a.

E.3 Natural image datasets: Additional performance metrics

In addition to AUROC (Fig. 3b), we computed AUPRC and FPR at 80% TPR for outlier detection with the natural image VAEs. AUPRC typically improved (Fig. 8a) and FPR decreased (Fig. 8b) for the BC and EV scores (orange and green symbols, respectively) compared to uncorrected likelihoods (blue symbols). As with the AUROC metric (Fig. 3b), outlier detection was generally poor with the CIFAR10 VAE.

Again, we report mean and standard deviation of the AUROC values across 6 runs (3 random weight initializations \times 2 train-validation splits) in Table 4.

Table 4: BC-LL AUROC values for VAEs trained with natural image datasets. Columns indicate training datasets (ID) and rows indicate test datasets (OOD).

SVHN	50.0 ± 0.0	84.83 ± 0.63	99.99 ± 0.0	87.11 ± 0.97	50.6 ± 0.42
CelebA	93.41 ± 0.15	50.0 ± 0.0	99.99 ± 0.0	88.79 ± 0.27	62.12 ± 0.66
CompCars	88.46 ± 0.48	88.46 ± 1.07	50.0 ± 0.0	89.63 ± 0.85	37.33 ± 0.75
GTSRB	91.86 ± 0.23	87.6 ± 0.2	99.98 ± 0.0	50.0 ± 0.0	65.47 ± 0.7
CIFAR10	90.8 ± 0.11	88.37 ± 0.31	99.98 ± 0.0	91.05 ± 0.53	50.0 ± 0.0
Noise	99.98 ± 0.01	99.99 ± 0.0	100.0 ± 0.0	100.0 ± 0.0	99.84 ± 0.01
OOD \uparrow \ ID \rightarrow	SVHN	CelebA	CompCars	GTSRB	CIFAR10

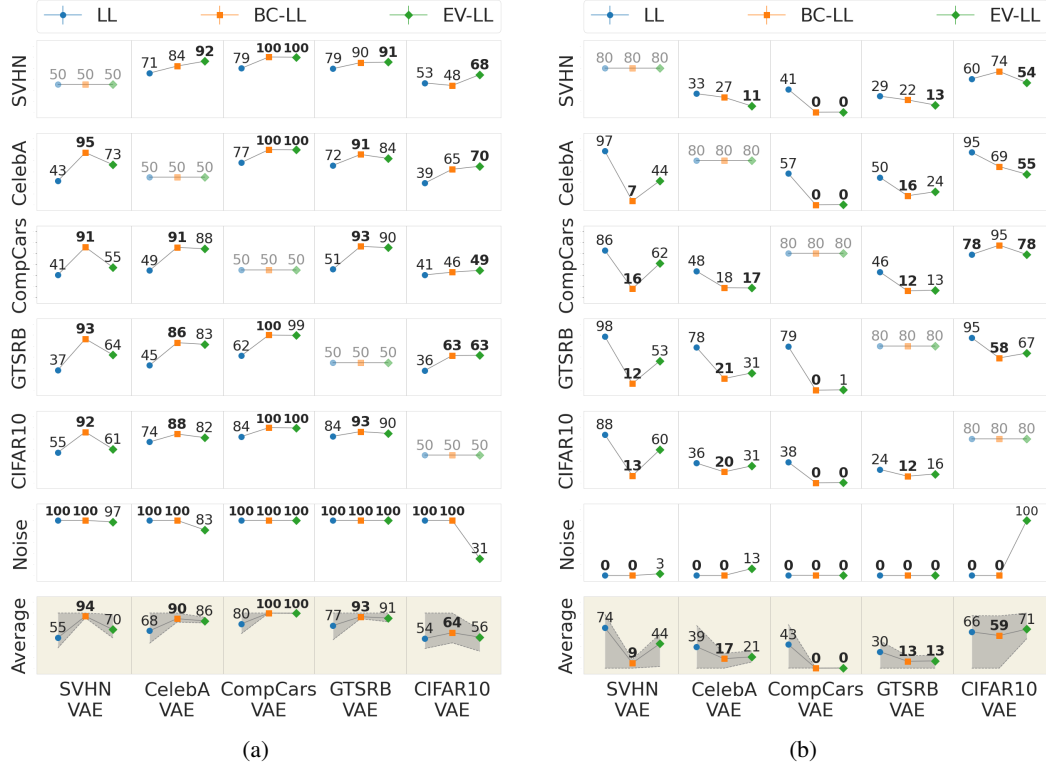


Figure 8: Same as in Figures 7a and 7b, but showing additional metrics for outlier detection, (a) AUPRC and (b) FPR at 80% TPR based on natural image VAE likelihoods. Other conventions are the same as in Figure 3b.

E.4 Dependence of outlier detection on contrast normalization

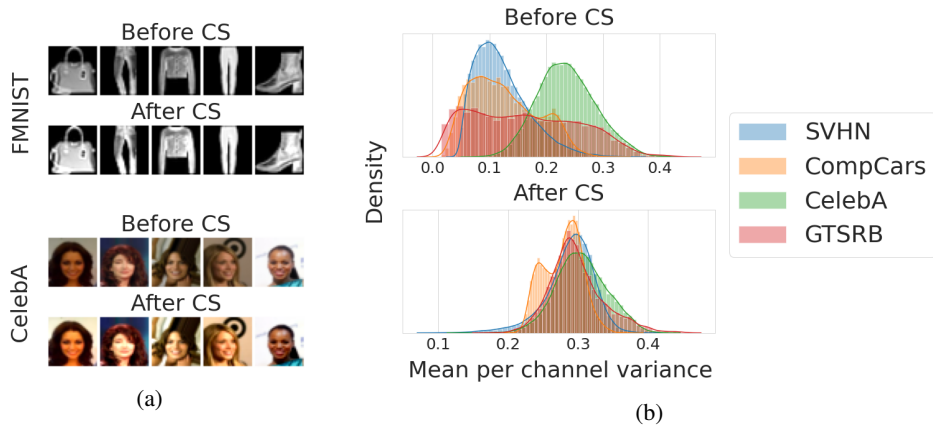
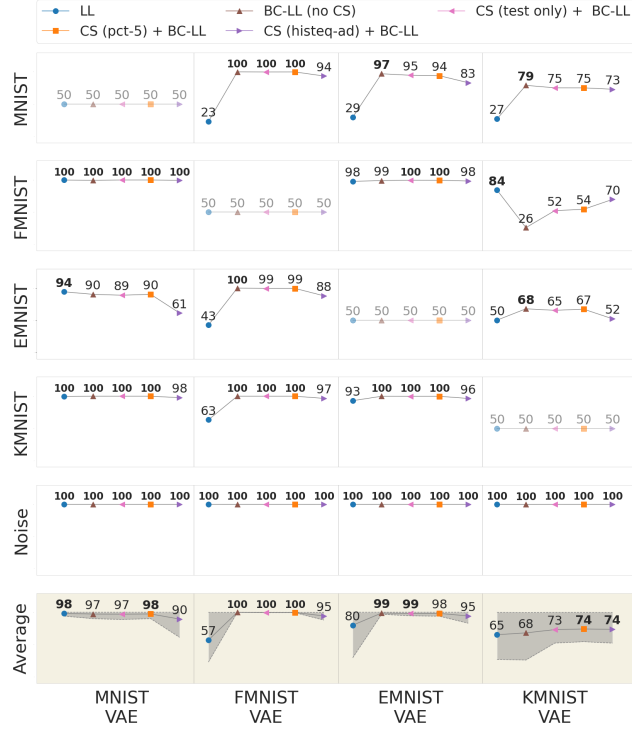
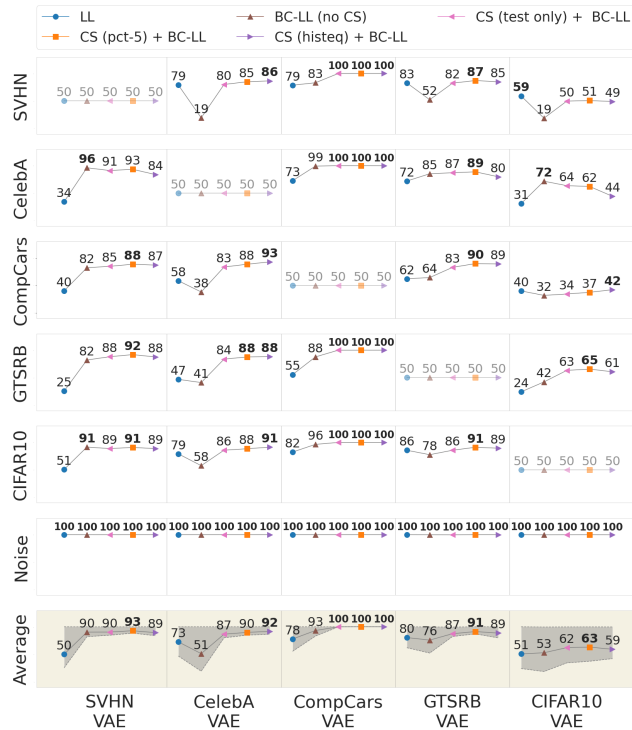


Figure 9: (a) Representative images from the Fashion-MNIST (top) and CelebA (bottom) datasets before (top row in each sub-panel) and after (bottom row in each sub-panel) contrast normalization (stretching). (b) Distributions of mean per-channel variance for the natural image datasets show greater overlap after (bottom), as compared to before (top), contrast stretching.



(a)



(b)

Figure 10: AUROC values for outlier detection based on (a) grayscale or (b) natural image VAE likelihoods, computed with no contrast normalization (BC-LL (no CS), brown symbols), with contrast stretching applied only at test time (CS (test only) + BC-LL, pink symbols), with contrast stretching applied at both train and test time (CS (pct-5) + BC-LL) and with histogram equalization instead of contrast stretching (CS (histeq) + BC-LL, magenta symbols), all with bias correction. Blue symbols: AUROC based on uncorrected likelihoods. An adaptive (local) histogram equalization algorithm (histeq-ad) was used for grayscale images because global histogram equalization produced unnatural variations in image contrast. Other conventions are the same as in Figure 3.

E.5 All-to-all comparison with other outlier detection approaches

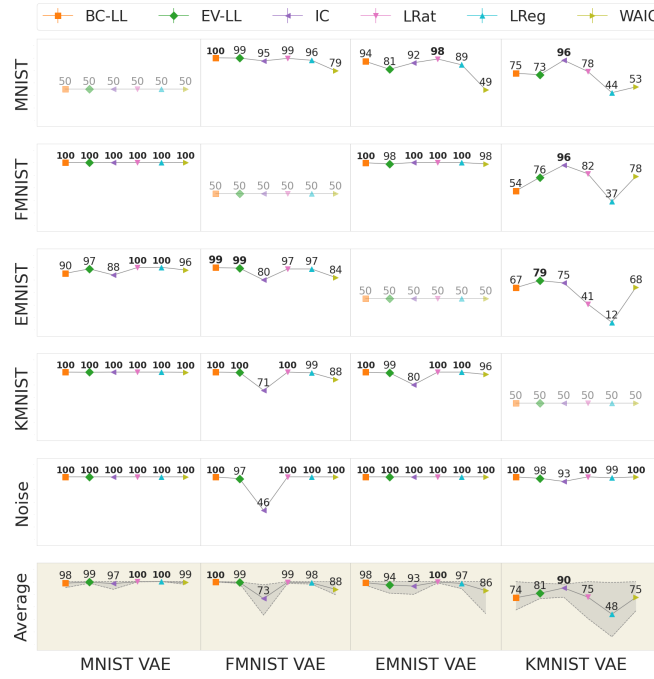


Figure 11: Same as Figure 5a but showing an all-versus-all comparison of AUROC values for outlier detection with four competing approaches for grayscale image VAEs. Columns: training datasets; Rows: test datasets. Other conventions are the same as in Figures 5a and 3a.

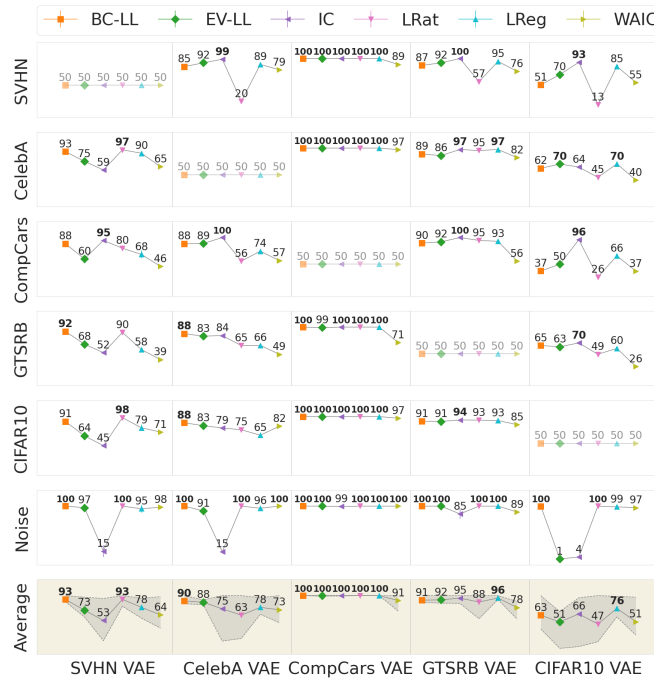


Figure 12: Same as Figure 5b but showing an all-versus-all comparison of AUROC values for outlier detection with four competing approaches for natural image VAEs. Columns: training datasets; Rows: test datasets. Other conventions are the same as in Figures 5b and 3b.

In the main text, we had presented comparisons of outlier detection AUROCs for the BC-LL and EV-LL scores with 4 other, competing approaches for specific VAEs (Figs. 5a and 5b). In Figures 11 and 12 we present all-to-all comparisons for all approaches with VAEs trained with the 4 grayscale and 5 natural image datasets and tested against each dataset (or noise) in its respective category.

E.6 Compute times and speedups: control analysis

In the main text, we had presented comparisons of BC-LL and EV-LL compute times and speedups with other, competing approaches, demonstrating the superior compute times of our metrics for outlier detection. Yet, two key differences could underlie these differences. First, whereas we have, by default, employed a VAE with $n_z=20$ hidden dimensions, competing approaches have employed VAEs with $n_z=100$ hidden dimensions. Second, our default VAE implementation is in TensorFlow 2.0 whereas competing approaches are all implemented in Pytorch.

To enable a fair comparison, we replicated the compute time analysis albeit, now: i) employing a VAE with $n_z=100$ hidden dimensions and ii) re-implementing our VAEs in Pytorch (1.8.0). All VAEs were then tested on identical hardware (Appendix H).

Again, with these precisely matched implementations, we observed evaluation times and speedups nearly identical with those reported in the main text (compare Fig. 5c-d with Fig. 13a-b).

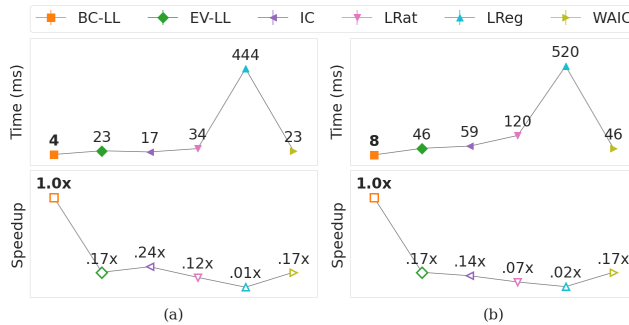


Figure 13: **(a)** Same as Figure 5c but showing compute times (top row) and speedups (bottom row) for BC-LL and EV-LL approaches using a grayscale image VAE with $n_z=100$ hidden dimensions implemented in Pytorch. Other conventions are the same as in Figure 5c. **(b)** Same as in panel (a) but showing compute times (top row) and speedups (bottom row) using a natural image VAE. Other conventions are the same as in Figure 5d.

Appendix F: Analysis of failure cases

F.1 Outlier detection with the KMNIST VAE

We analyze the single failure case of outlier detection of Fashion-MNIST samples with the KMNIST VAE. For this VAE, AUROC for outlier detection of Fashion-MNIST samples was better with uncorrected likelihoods as compared to that with bias-corrected likelihoods (Fig. 3a, second row, last column). Was bias correction, therefore, ineffective for the KMNIST VAE?

We propose otherwise. First, bias correction improved outlier detection relative to uncorrected likelihoods, when the KMNIST VAE was tested against other outlier datasets (e.g. MNIST or EMNIST; Fig. 3a, first and third rows, last column). Our scores also performed on par with, or better than all but one competing approach (IC) with this dataset (Fig. 5a, Average, bottom row, last column). Second, when we plotted the most typical samples, based on highest uncorrected likelihoods (Fig. 14a, top), we discovered that these were heavily biased toward images with many black pixels. Following bias correction, however, the highest likelihood samples now resembled typical Japanese alphabet characters (Fig. 14a, bottom). In other words, our BC-LL score indeed ameliorated key biases with vanilla likelihoods.

We analyze this failure case further by plotting Fashion-MNIST samples assigned the highest log likelihoods by the KMNIST VAE (Fig. 14b, top) and their reconstructions (Fig. 14b, bottom). We

observed that these typically comprised items of clothing, with relatively uniform shading, that occupied nearly the entire frame of the image (Fig. 14b, top), and were reconstructed reasonably well by the KMNIST VAE. Nonetheless, these reconstructions contained “gaps” (dark pixels) in several places, visually mimicking Japanese alphabet characters (Fig. 14b, bottom). We propose that the KMNIST VAE learned a set of features general enough to reconstruct specific Fashion-MNIST samples, thereby resulting in poor outlier detection with this dataset.

To further verify this claim we also plotted Fashion-MNIST samples assigned the highest log likelihoods by the MNIST VAE (Fig. 14c, top) and their reconstructions (Fig. 14c, bottom). The MNIST VAE was unable to reconstruct Fashion-MNIST samples accurately, thereby yielding low likelihoods for these samples and, therefore, resulting in better outlier detection.

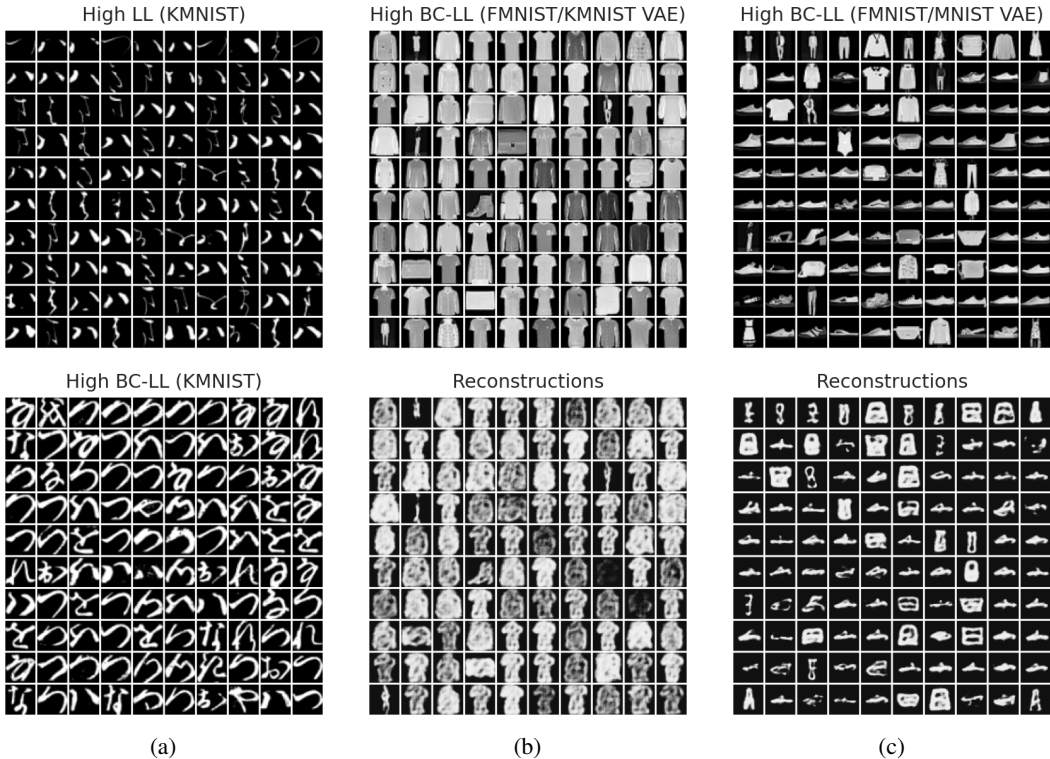


Figure 14: (a) 100 KMNIST samples assigned the highest log likelihoods by the KMNIST VAE before (top row) and after (bottom row) bias correction. (b) 100 Fashion-MNIST samples assigned the highest log likelihoods by the KMNIST VAE following bias correction (top row) and their reconstructions (bottom row). (c) 100 Fashion-MNIST samples assigned the highest log likelihoods by the MNIST VAE following bias correction (top row) and their reconstructions (bottom row).

F.2 Outlier detection with the CIFAR-10 VAE

Our BC-LL and EV-LL scores approached or exceeded state-of-the-art accuracies for outlier detection with multiple grayscale and natural image datasets (Figs. 5, 11, 12). Nonetheless, VAEs trained on the CIFAR-10 dataset yielded relatively low AUROC values ranging from 37-65 with bias correction and 50-70 with ensemble variance (Fig. 12, last column, all outlier datasets except Noise). Interestingly, other approaches based on VAE likelihoods also performed relatively poorly with this dataset (Fig. 12, last column)

We hypothesized that this failure could be due to the heterogeneity of the CIFAR-10 dataset: this dataset comprises 10 different categories of images, which are both visually and semantically unrelated to each other (e.g. airplanes, deer, frogs, ships). We tested this hypothesis by training four category-specific VAEs with images from four CIFAR-10 image categories (Airplane, Ship, Frog and Deer) and tested them against the other datasets. Outlier detection performance improved, both with the BC-LL and EV-LL scores for the VAEs trained on specific categories of images (Fig. 15, last 4

columns) relative to the one trained with all categories of images (Fig. 15, first column). On average, category-specific outlier detection with the BC-LL score improved by between 6-20 points (Fig. 15, last row) for the individual categories compared to the VAE trained on all categories. Similarly EV-LL based outlier detection improved by between 9-31 points.

These results suggest that the heterogeneity in CIFAR-10 categories was, in part, responsible for overall poor outlier detection with this dataset. Yet, even with these category-specific CIFAR-10 VAEs, outlier detection performance did not reach the superlative levels of accuracy that it did with the other natural image datasets (e.g. Fig 12, CompCars, GTSRB).

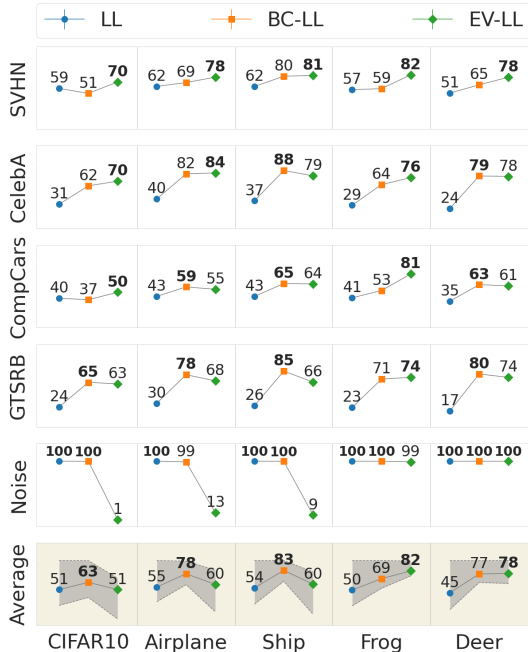


Figure 15: AUROC values for outlier detection based on VAEs trained with specific categories of images in the CIFAR-10 dataset. (Leftmost to rightmost columns) VAEs trained with all CIFAR-10 image categories, Airplane images, Ship images, Frog images and Deer images. Each row is an outlier dataset. Other conventions are the same as in Figure 3b.

Why do VAE likelihoods fail when other classifier-based outlier detection methods (e.g. [12]) succeed? To answer this question, we note that there is a key difference between VAEs and deep CNN classifiers. Deep CNN classifiers transform the input image into a spatially-invariant (typically translation-invariant) feature representation, on which a classification decision must be made. Even though the VAE encoder employs a CNN that achieves such a transformation, the VAE decoder needs to reconstruct the entire image pixel-for-pixel. Consequently, VAEs can ill-afford to ignore spatial relationships among the features and their positions relative to a coordinate frame that is locked to the “edge” of the image. In other words, to optimize its objective, a VAE must care not only about “what” features are present in an image, it must also encode “where” these features are positioned relative to each other and, importantly, relative to the image’s bounding box. We propose that datasets in which such spatial relationships do not occur consistently (e.g. CIFAR-10) are particularly unsuited for outlier detection with VAEs.

We test this prediction with a simple set of experiments. We plotted the bias corrected likelihoods for representative VAEs (GTSRB, CelebA, CompCars), each following a simple affine transformation: a) x/y translation (uniform random shift of $\pm 0-10$ pixels along both x and y directions) (Fig. 16, left, GTSRB), b) reflection about the horizontal axis (Fig. 16, middle, CelebA) or c) rotation by 90 degrees anti-clockwise (Fig. 16, right, CompCars). Each of these affine operations sufficed to hoodwink the VAEs into treating their, respective, inlier images as outliers: the VAEs consistently assigned lower likelihoods for these translated, reflected or rotated in-distribution images (Fig. 16, orange distributions), as compared to their original counterparts (Fig. 16, blue distributions). This was particularly surprising for the case of perturbation by translation, to which the encoder CNN

typically learns invariance. In sum, even though all image features were exactly (or nearly) identical between the original and affine transformed images, VAE outlier detection failed because perturbed image features were in novel spatial positions relative to the edge of the image.

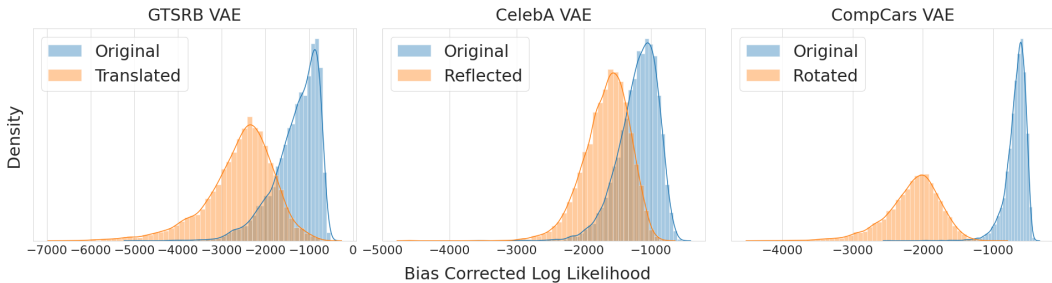


Figure 16: **(Left)** GTSRB VAE likelihoods (bias corrected) for the original images (blue distribution) or for the images following small, random wrap-around x/y translations (orange distribution). **(Middle)** CelebA VAE likelihoods (bias corrected) for the original images (blue distribution) or for the images flipped vertically (orange distribution). **(Right)** CompCars VAE likelihoods (bias corrected) for the original images (blue distribution) or for the images rotated by 90 degrees anti-clockwise (orange distribution).

We discuss a few possibilities to overcome this limitation. One solution is to train the VAE, not directly on natural images, but after transforming them into a spatially-invariant “semantic” feature representation. Indeed, a recent study ([10], their Appendix N) attempted precisely this experiment with deep generative (Flow) models using features from a pretrained EfficientNet model, and showed that such features enabled robust outlier detection, even with the CIFAR-10 dataset. A second possibility is to perturb the output variously [6, 1] and develop reconstruction error metrics that are invariant to these perturbations in the input data. These additional remedies could enable VAEs to be employed in real-world settings, for example, involving streams of natural images (e.g. videos).

Appendix G: Bias correction for the categorical VAE visible distribution

We have demonstrated a theoretically-motivated bias correction that works with the Bernoulli and continuous Bernoulli visible distributions for the decoder (Appendix B). Nonetheless, the “categorical distribution” is also a popular choice of visible distribution for various generative models, including VAEs [30, 23] and autoregressive models like PixelCNN/PixelCNN++ [24]. Here we describe a method to compute bias correction for likelihoods for VAEs with the categorical visible distribution, and demonstrate significant improvements in outlier detection with this correction.

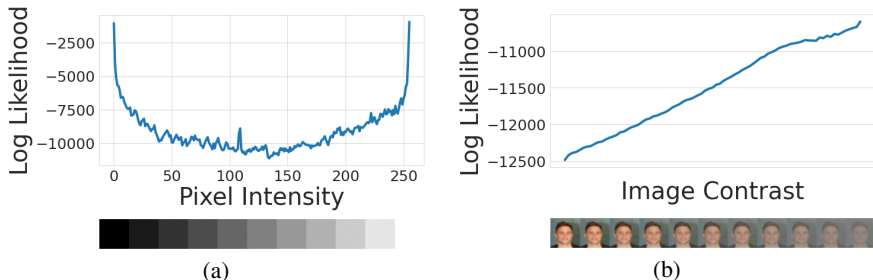


Figure 17: Same as Figs. 1c and 1f in the main text, but showing the log likelihood variation with either pixel intensity **(a)** or image contrast **(b)** for a VAE trained with the categorical visible distribution. Other conventions are the same as in Figs. 1c and 1f.

To illustrate the need for the bias correction, first, we computed the empirical bias in the log likelihood for images with various uniform pixel intensities (0-255), for a CelebA VAE with a categorical visible distribution (Fig. 17a). We observed a U-shaped profile, similar to that observed for VAEs trained with the continuous Bernoulli visible distribution (Fig. 1c).

Second, we computed the bias for images of different image contrasts. Again, varying image contrasts produced systematic biases in reconstruction error (Fig. 17b). But – surprisingly – this bias was in a direction opposite to that observed with the continuous Bernoulli distribution (Figure 1f). Specifically, this bias increased systematically as image contrast decreased, in line with observations by Nalisnick et al (2019) [18].

These experiments indicate that biases in deep generative model likelihoods, arising from low-level pixel statistics, critically depend on the decoder visible distribution.

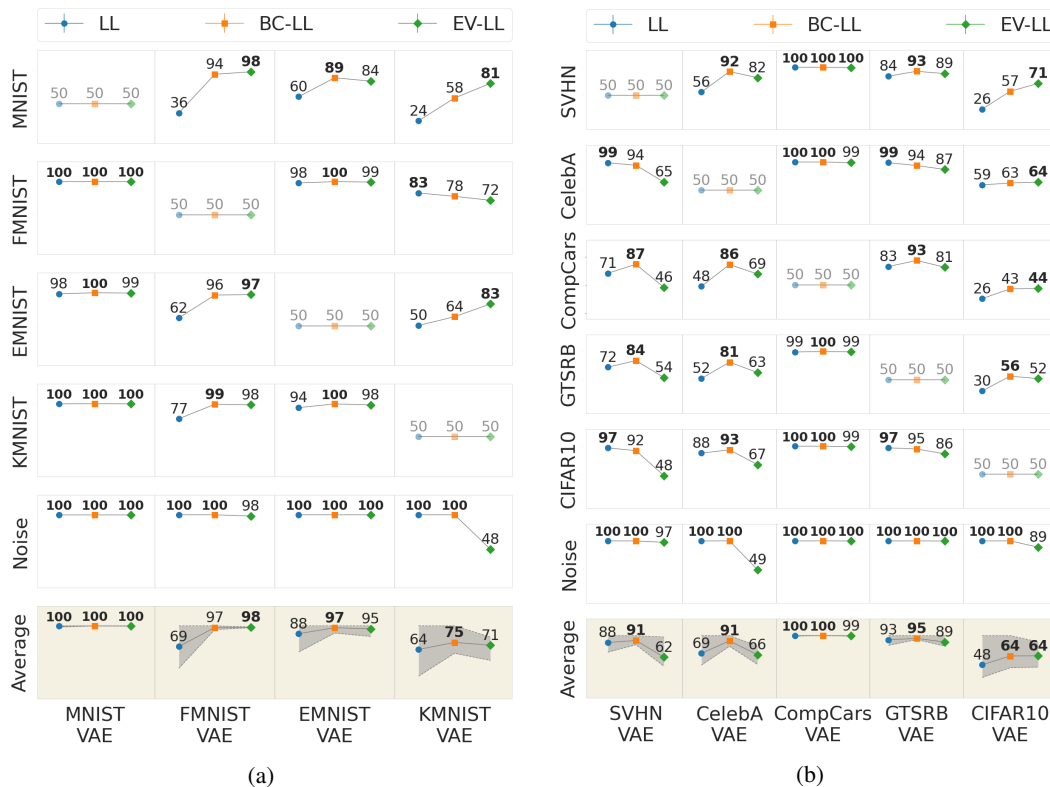


Figure 18: Outlier detection with bias corrected likelihoods and ensemble variance for the categorical VAE visible distribution with (a) grayscale or (b) natural image datasets. Other conventions are the same as in Figure 3.

Next, we corrected for this bias with the following theoretically-grounded approach. For each VAE, we computed the average categorical distribution output for every target pixel value (0-255) employing all of the training (inlier) samples for that VAE. Then, for each test sample, we computed the correction term for the negative reconstruction error as its average value across pixels, under the categorical visible distribution. This procedure is described in detail in Algorithm 1.

We demonstrate the effectiveness of this correction with an all-to-all comparison of outlier detection with VAEs trained on the 4 grayscale (or 5 natural image) datasets and tested against each outlier dataset in its respective category (or noise). As shown in Figure 18 (last row), outlier detection improved, on average, in every case with our bias correction approach. More generally, such a theoretical analysis and empirical correction may be relevant for improving outlier detection with other categories of deep generative models also [24].

Algorithm 1: Bias correction for the categorical visible distribution

Data: Training Set $\mathbf{X} = \{\mathbf{x}_1, \mathbf{x}_2, \dots, \mathbf{x}_n\}$ with \mathbf{x}_p of shape $32 \times 32 \times nc$ (no. of channels), Encoder Parameters ϕ , and Decoder Parameters θ

Result: Log Correction Factor $\mathbf{C} : (v, k) \rightarrow \text{Float}$ for $v = 0, 1, \dots, 255$ and $k = 1, 2, \dots, nc$

Init: Map $\mathbf{A} : (v, k) \rightarrow \text{EmptyList}$ for $v = 0, 1, \dots, 255$ and $k = 1, 2, \dots, nc$

for $\mathbf{x}_p \in \mathbf{X}$ **do**

- Init:** Map $\mathbf{B} : (v, k) \rightarrow \text{EmptyList}$ for $v = 0, 1, \dots, 255$ and $k = 1, 2, \dots, nc$
- $\mathbf{z} \sim q_\phi(\mathbf{z}|\mathbf{x}_p)$
- for** $i \leftarrow 1$ **to** 32, $j \leftarrow 1$ **to** 32, $k \leftarrow 1$ **to** nc **do**

 - | Append $p_\theta^{ijk}(x_p^{ijk}|\bar{\mathbf{z}})$ to $\mathbf{B}(x_p^{ijk}, k)$

- end**
- for** $v \leftarrow 0$ **to** 255, $k \leftarrow 1$ **to** nc **do**

 - | Append $\text{Mean}(\mathbf{B}(v, k))$ to $\mathbf{A}(v, k)$

- end**

end

Init: Map $\mathbf{C} : (v, k) \rightarrow 0$ for $v = 0, 1, \dots, 255$ and $k = 1, 2, \dots, nc$

for $v \leftarrow 0$ **to** 255, $k \leftarrow 1$ **to** nc **do**

- | $\mathbf{C}(v, k) \leftarrow \text{Log}(\text{Mean}(\mathbf{A}(v, k)))$

end

Appendix H: Reproducibility checklist

Data. All datasets used in this study are publicly available, and sources are provided in Appendix C.

Experimental results. Evaluation metrics (AUROC, AUPRC, FPR@80%TPR) are standard outlier detection metrics in literature [23, 17, 12, 3], and described in Appendix D. Train/test/validation splits and selection of hyperparameters are all described, at the appropriate places (Appendix C, Table 4).

Code. We have described, in full detail, the implementation of the bias-corrected likelihood and ensemble variance metrics introduced in this study (Section 3, Appendix B, Appendix G) for ready reproducibility. We have also specified in detail all dependencies including the names and versions of relevant software libraries and frameworks (Appendices A, C, D, E.6). We plan to publish the code soon.

Compute Environment. All experiments were performed in the cloud with individual jobs equipped with an NVIDIA Tesla V100 and 32GB of memory.